ACSNANO

www.acsnano.org

ARTICLE

Impacts of Oxygen Vacancies on Zinc Ion Intercalation in VO_2

Zhaoqian Li, Yingke Ren, Lie Mo, Chaofeng Liu, Kevin Hsu, Youcai Ding, Xianxi Zhang, Xiuling Li, Linhua Hu,* Denghui Ji,* and Guozhong Cao*

Cite This: *ACS Nano* 2020, 14, 5581−5589

Read Online

ACCESS | Metrics & More | Article Recommendations | Supporting Information

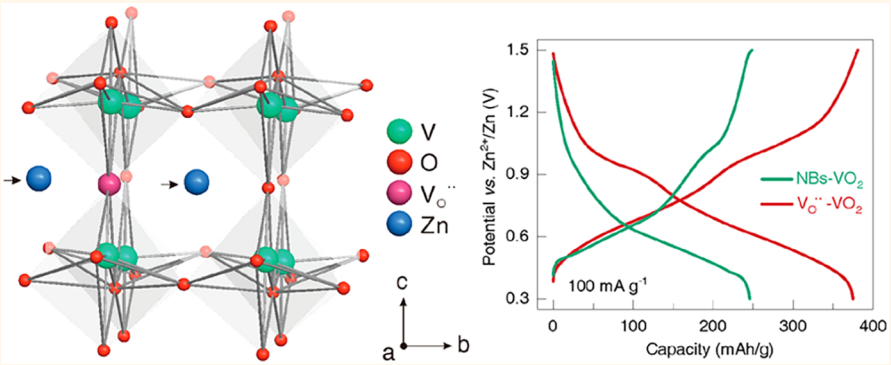

ABSTRACT: **The aqueous zinc ion battery has emerged as a promising alternative technology for large-scale energy storage due to its low cost, natural abundance, and high safety features. However, the sluggish kinetics stemming from the strong electrostatic interaction of divalent zinc ions in the host crystal structure is one of challenges for highly efficient energy storage. Oxygen vacancies ($V_O^{\bullet\bullet}$), in the present work, lead to a larger tunnel structure along the *b* axis, which improves the reactive kinetics and enhances Zn-ion storage capability in VO_2 (B) cathode. DFT calculations further support that $V_O^{\bullet\bullet}$ in VO_2 (B) result in a narrower bandgap and lower Zn ion diffusion energy barrier compared to those of pristine VO_2 (B). $V_O^{\bullet\bullet}$-rich VO_2 (B) achieves a specific capacity of 375 mAh g^{-1} at a current density of 100 mA g^{-1} and long-term cyclic stability with retained specific capacity of 175 mAh g^{-1} at 5 A g^{-1} over 2000 cycles (85% capacity retention), higher than that of VO_2 (B) nanobelts (280 mAh g^{-1} at 100 mA g^{-1} and 120 mAh g^{-1} at 5 A g^{-1}, 65% capacity retention).**

KEYWORDS: *VO_2, oxygen vacancies, defects, cathode materials, aqueous zinc ion batteries*

Lithium ion batteries efficiently power portable electronics and electric vehicles in modern society owing to their high energy density. However, concerns about their cost and safety limit their large-scale applications such as in stationary grids.[1,2] Rechargeable batteries relied on multivalent cations such as Al^{3+},[3] Mg^{2+},[4] Zn^{2+},[5−8] with nonflammable aqueous electrolytes are potential alternatives. Their benefits include the inherent safety, affordable cost, and feasible fabrication.[9−11] Zn^{2+} has similar ionic radii (0.74 Å) with Li^+ (0.76 Å), low redox potential (−0.76 V *vs* standard hydrogen electrode), and high gravimetric and volumetric capacities (820 mAh g^{-1} and 5855 mAh cm^{-3}), leading to increasing attention and research work on aqueous zinc ion batteries (ZIBs).[12] So far, a number of cathode materials for ZIBs have been studied, including manganese-based oxides,[13,14] vanadium-based composites,[15−19] Prussian blue and its analogues,[20−23] transition-metal dichalcogenides,[24,25] and organic compounds.[26,27] As one of the important members of the vanadium oxide family, VO_2 (B) has been investigated as an electrode material for Zn ion storage owing to its open tunnel-like frameworks (0.34, 0.82, and 0.52 nm^2 along the *a*, *b*, and *c* axis, respectively).[28−32] For example, Ding *et al.*[32] studied VO_2 (B) nanofibers as cathode for ZIBs and achieved a high reversible capacity of 357 mAh g^{-1} at 0.25 A g^{-1} and outstanding rate capability of 171 mAh g^{-1} at 51.2 A g^{-1}. Chen *et al.*[33] developed VO_2 nanorods as cathodes for aqueous ZIBs,

Received: December 18, 2019
Accepted: May 11, 2020
Published: May 11, 2020

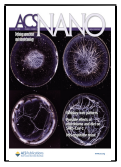

https://dx.doi.org/10.1021/acsnano.9b09963
ACS Nano 2020, 14, 5581−5589

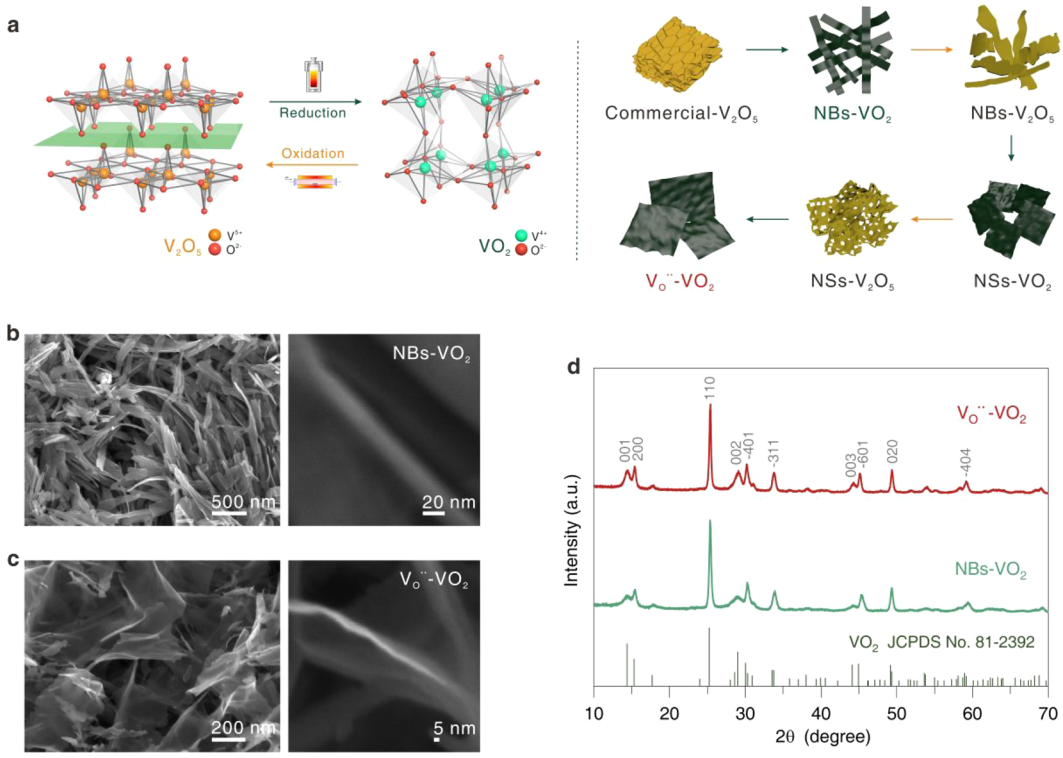

Figure 1. (a) Schematic illustration of the synthesis process. SEM images of NBs–VO_2 (b) and $V_O^{\bullet\bullet}$–VO_2 (c). (d) XRD patterns of NBs–VO_2 and $V_O^{\bullet\bullet}$–VO_2.

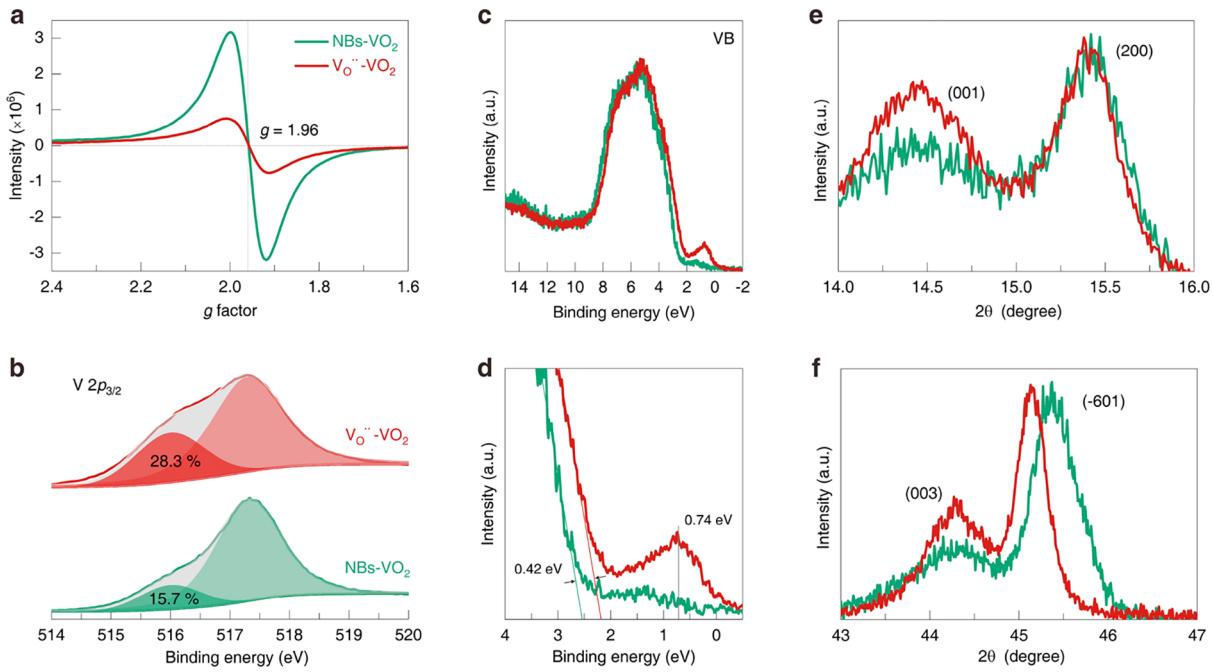

Figure 2. (a) EPR spectra of NBs–VO_2 and $V_O^{\bullet\bullet}$–VO_2. The weaker the peak intensity, the higher the concentration of $V_O^{\bullet\bullet}$. (b–d) XPS spectra of NBs–VO_2 and $V_O^{\bullet\bullet}$–VO_2. (b) V2$p_{3/2}$ spectra. The significantly line shape changes indicate much more V2p suboxide formed in $V_O^{\bullet\bullet}$–VO_2 than NBs–VO_2. (c) Full valence-band and (d) zoomed in view of the low binding energy region. For the $V_O^{\bullet\bullet}$–VO_2, the enhanced peak appeared at binding energy 0.74 eV associates with the formation of $V_O^{\bullet\bullet}$. (e, f) Selected XRD patterns of the (200) and (−601) diffraction peaks that compare NBs–VO_2 and $V_O^{\bullet\bullet}$–VO_2. The lower angle shift of peak positions suggests the expanded lattice spacings.

which displayed a discharge capacity of 325.6 mAh g^{-1} at 0.05 A g^{-1} and cyclic stability of 86% capacity retention after 5000 cycles at 3.0 A g^{-1}. However, an obstacle in boosting zinc-ion storage performance is the slow mobility of the Zn^{2+} in the host materials because of the strong electrostatic interaction between divalent Zn ions and the host crystal structures.[34]

One of the strategies is to introduce structural water and interlayer metal cations between the adjacent layers, which

https://dx.doi.org/10.1021/acsnano.9b09963
ACS Nano 2020, 14, 5581−5589

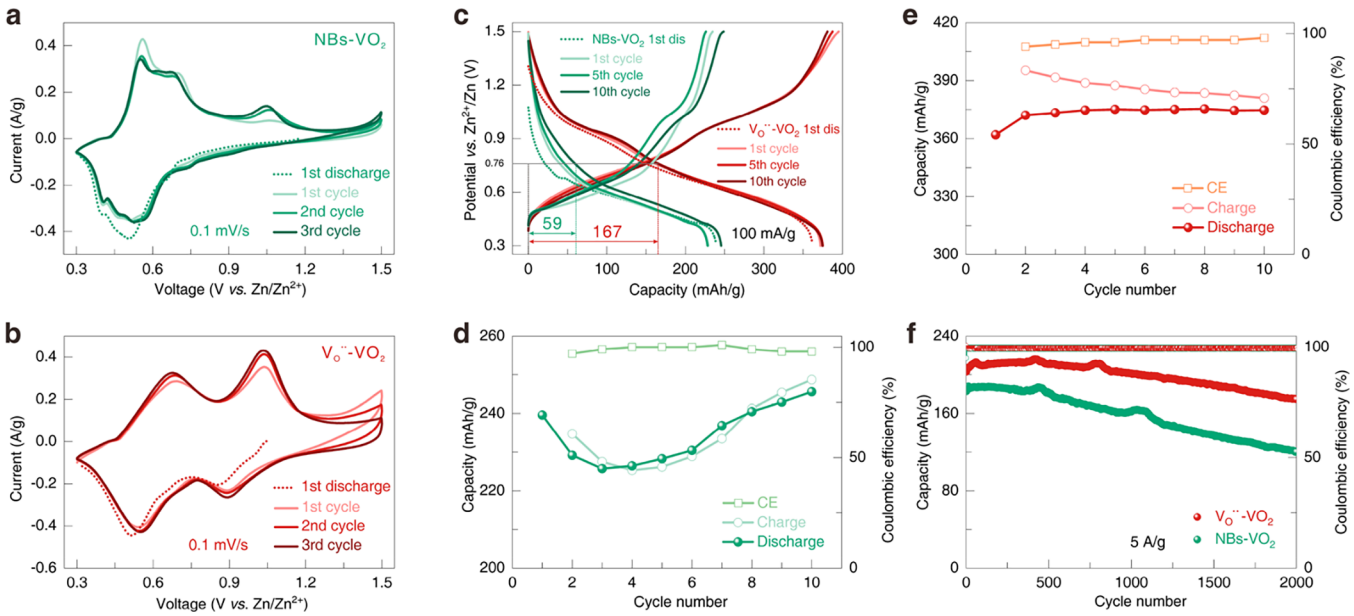

Figure 3. (a, b) Cyclic voltammogram (CV) curves (sweep rate: 0.1 mV s^{-1}) of NBs−VO_2 (a) and $V_O^{\bullet\bullet}$−VO_2 (b). (c−e) galvanostatic charge/discharge profiles and Coulombic efficiency profiles at 100 mA g^{-1} for NBs−VO_2 (c, d) and $V_O^{\bullet\bullet}$−VO_2 (c, e) in the first 10 cycles. (f) Long-term cycling performance at 5 A g^{-1} for NBs−VO_2 and $V_O^{\bullet\bullet}$−VO_2.

have been studied in vanadium-based cathodes.[35−38] The structural water acts as an electrostatic shield for Zn^{2+}, broadens the diffusion tunnels, and alters the working potential.[37,38] Inserted metal cations can open the crystal interlayer spacing, ensuring fast and reversible Zn^{2+} insertion/extraction.[35,36] Another strategy is to introduce defects such as cationic or anionic vacancies in the crystal lattices because defects are beneficial to suppress the needless phase transition and provide more activated sites for enhanced zinc ion storage capacity.[39−44] It has been demonstrated that oxygen vacancies ($V_O^{\bullet\bullet}$) can increase the interlayer spacings of metal oxides and improve their ion diffusion kinetics, favoring the fast ion insertion and extraction.[44,45]

In this paper, $V_O^{\bullet\bullet}$-rich VO_2 (B) ($V_O^{\bullet\bullet}$−VO_2) were synthesized through a repeated phase transition processing, and the impacts of $V_O^{\bullet\bullet}$ on crystal structure, electrochemistry, and zinc ion storage properties of VO_2 (B) were systematically studied. The $V_O^{\bullet\bullet}$ concentrations in VO_2 (B) were found to greatly affect the crystal structure and band structure and led to various electrochemical properties. Density functional theory (DFT) calculations give insight regarding crystal structure, band structure, and zinc ion diffusion properties for $V_O^{\bullet\bullet}$-rich VO_2 (B). Experimental results combined with DFT calculations reveal that $V_O^{\bullet\bullet}$ in VO_2 (B) could lead to improved electrical conductivity and expanded ion diffusion tunnels, enabling fast and reversible Zn^{2+} storage.

RESULTS AND DISCUSSION

Figure 1a illustrates how VO_2 nanobelts (NBs−VO_2) were synthesized by reducing commercial V_2O_5 with a solvothermal method. SEM images (Figure 1b) showed that the sample consists of nanobelts with a thickness of ∼15 nm. A repeated phase transition method building on the reduction and oxidation reaction between V_2O_5 and VO_2 was used to form $V_O^{\bullet\bullet}$−VO_2 (Figures 1a and S1−S6. The detailed synthesis process is described in the Supporting Information).[32,33,46,47] Figure 1c shows the SEM images of $V_O^{\bullet\bullet}$−VO_2; after the twice repeated phase transition operation, the morphology transforms from nanobelts (NBs−VO_2) to nanosheets with a thickness of ∼5 nm. XRD patterns confirmed both NBs−VO_2 and $V_O^{\bullet\bullet}$−VO_2 retained the same crystal structure (Figure 1d) and all diffraction peaks are indexed well with the standard monoclinic VO_2 (B) (JCPDS card no. 81−2392).

Tetravalent V ion is paramagnetic while trivalent V ion is electron paramagnetic resonance (EPR) silent because of the combination of the integer spin number and large zero-field splitting;[48,49] thus, the EPR intensity changes of tetra V cation demonstrate the variety of defect state concentration in both VO_2 samples. Signals with a g value of 1.96 were detected in both VO_2 samples (Figure 2a), corresponding to tetravalent V ion.[50,51] $V_O^{\bullet\bullet}$−VO_2 showed a lower signal intensity than that of NBs−VO_2, demonstrating the V^{4+} has a different concentration in the two samples. That is, the decreased signals in VO_2 samples represent the decrease concentration of V^{4+} while increase concentration of V^{3+} since trivalent V is EPR silent and has no EPR signal.[48,49] In fact, V_2O_3 phase was not detected in the XRD patterns (Figure 1d), the appearance of V^{3+} implies the formation of nonstoichiometric VO_2, which is associated with the $V_O^{\bullet\bullet}$.[52] The increased proportion of V^{3+} demonstrates more $V_O^{\bullet\bullet}$ in $V_O^{\bullet\bullet}$−VO_2.[52−54] The different quantity of V valence state directly affects surface chemical state of VO_2 samples which can be confirmed by XPS. As shown in Figure 2b, V $2p_{3/2}$ XPS spectra identified the increased proportion of V^{3+} in $V_O^{\bullet\bullet}$-VO_2.[55,56] According to the intensity ratio of V^{3+} (Figure 2b), $V_O^{\bullet\bullet}$−VO_2 and NBs−VO_2 samples are confirmed to be $VO_{1.86}$ and $VO_{1.92}$, respectively. After introducing $V_O^{\bullet\bullet}$, a new state in the valence band spectra region (Figures 2c,d) formed with a peak at binding energy of 0.74 eV. The peak intensity in $V_O^{\bullet\bullet}$−VO_2 is higher than NBs−VO_2, demonstrating a high concentration of $V_O^{\bullet\bullet}$. Meanwhile, a 0.42 eV shift toward lower binding energy is observed. Similar with the lattice disorder and doping,[57,58] a large amount of $V_O^{\bullet\bullet}$ in semiconductors could lead to midgap states which induce a consecutive extension to the conduction band edge, resulting in a reduced binding energy of valence

https://dx.doi.org/10.1021/acsnano.9b09963
ACS Nano 2020, 14, 5581−5589

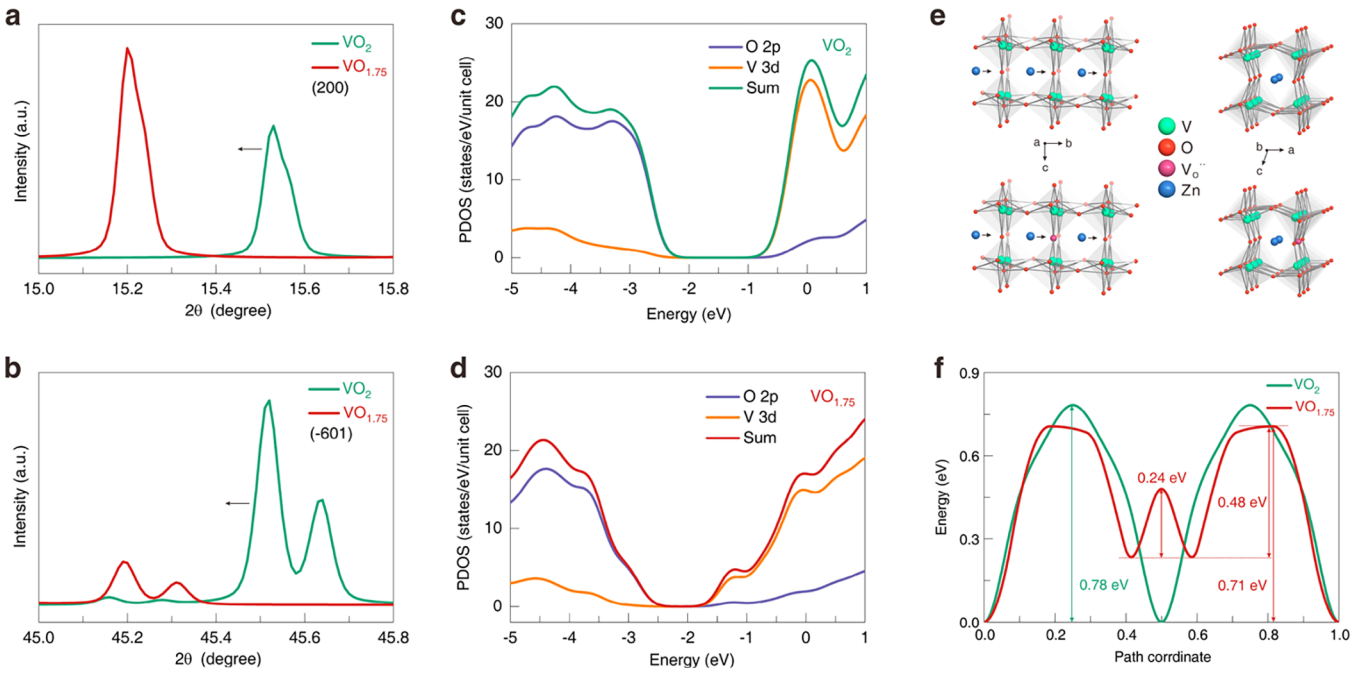

Figure 4. (a, b) Enlargement of calculated XRD patterns of the (200) and (−601) peaks to show the shift trend of $VO_{1.75}$ compared with VO_2. (c, d) Projected density of states (PDOS) of VO_2 (c) and $VO_{1.75}$ (d). (e) Zinc ions diffusion pathways along the b tunnel in VO_2 and $VO_{1.75}$. (f) Calculated Zn ion diffusion energy barriers in VO_2 and $VO_{1.75}$.

electrons.[57−60] One advantage of these $V_O^{\bullet\bullet}$ is that they offer jumping sites for charge transport, accelerating the electrochemical properties.[43,60] With increasing $V_O^{\bullet\bullet}$, another significant structural effect is changing the lattice constant of metal oxide, leading to the shrink or expansion of crystal planes or tunnels.[44,45] The expansion of crystal planes of tunnels will facilitate the diffusion of ions, *e.g.*, Li^+,[44,61] Na^+,[45,62] Zn^{2+}.[7,63] Parts e and f of Figure 2 show that (200) and (−601) diffractions shifted to lower angles from NBs−VO_2 to $V_O^{\bullet\bullet}$−VO_2, revealing the broadening of the corresponding crystal planes. The XRD diffractions shift in $V_O^{\bullet\bullet}$−VO_2 means the changes of lattice parameters as revealed by the DFT calculations (Table S1). Introducing $V_O^{\bullet\bullet}$ lead to the increase of lattice constant a and c, corresponding to the expansion of b tunnels, which is the largest and main diffusion tunnels for ions in VO_2 (B).[32,33,64]

Parts a and b of Figure 3 are curves of NBs−VO_2 and $V_O^{\bullet\bullet}$−VO_2. An additional peak at ∼0.9 V (ending at ∼0.76 V) for $V_O^{\bullet\bullet}$−VO_2 appears during the intercalation process in comparison with NBs−VO_2. The extra peak is probably ascribed to the $V_O^{\bullet\bullet}$ because the main distinction for NBs−VO_2 and $V_O^{\bullet\bullet}$−VO_2 is the different $V_O^{\bullet\bullet}$ contents as certified by EPR and XPS analysis. A similar case has been reported by Kim *et al.* in reduced MoO_3 (R-MoO_{3-x}).[44] The presence of $V_O^{\bullet\bullet}$ causes an additional deintercalation peak at ∼3.0 V compared with the full oxidized MoO_3 (F-MoO_3). In this work, the different concentrations of $V_O^{\bullet\bullet}$ in NBs−VO_2 and $V_O^{\bullet\bullet}$−VO_2 cause the different kinds of CV curves of Zn^{2+} intercalation and deintercalation in both samples. With the increase of $V_O^{\bullet\bullet}$, the deintercalation peak intensity at ∼1.0 V was enhanced, and an additional intercalation peak at ∼0.9 V appeared in $V_O^{\bullet\bullet}$−VO_2. The phenomenon together with the above XRD results show that the concentration of $V_O^{\bullet\bullet}$ in VO_2 might have a threshold value to influence the crystal structure and electrochemical properties. To confirm this extra peaks pair is associated with $V_O^{\bullet\bullet}$, we conducted the CV tests of VO_2 nanosheets (NSs−VO_2) sample whose $V_O^{\bullet\bullet}$ content is between the NBs−VO_2 and $V_O^{\bullet\bullet}$−VO_2 (Figure S7a). As shown in Figure S7b, NSs−VO_2 shows a pair of peaks at high voltage similar to $V_O^{\bullet\bullet}$−VO_2, but the peak intensity ratio of high voltage to low voltage is lower than that of $V_O^{\bullet\bullet}$−VO_2. XRD characterization (Figure S8a) of the $V_O^{\bullet\bullet}$−VO_2 electrode before discharging confirmed that no phase transition occurred in the fabrication process, including the grinding, mixing, coating, and drying process, while the XRD pattern recovered back to VO_2 (B) after being recharged to 1.5 V, verifying the final V cation in the cathode is tetravalent rather than V^{5+}, which agrees well with previous reports in VO_2 cathodes.[32,56] Zn 2*p* XPS spectra at different discharge states confirmed the discharge process of the $V_O^{\bullet\bullet}$−VO_2 electrode is zinc ions insertion (Figure S8b). Until now, no work has been reported to discuss and compare this distinct electrochemical characteristic of VO_2. VO_2 nanofibers with poor crystallinity reported by Ding *et al.*[32] showed the same CV curve with our $V_O^{\bullet\bullet}$−VO_2, while VO_2 nanorods with large particle size and good crystallinity by Chen *et al.*[33] still have characteristics similar to those of NBs−VO_2. However, the precise formation mechanism of this additional pair of peaks using $V_O^{\bullet\bullet}$ rich−VO_2 as the cathode for ZIBs is unclear and demands further detailed investigation.

Figure 3c shows the galvanostatic charge−discharge curves. In line with the CV curves, $V_O^{\bullet\bullet}$−VO_2 exhibits an extra discharge and longer charge plateau compared with NBs−VO_2 at the voltage region >0.76 V (Figure 3c). Comparing the 10th discharge capacity of both samples, the extra discharge region enables $V_O^{\bullet\bullet}$−VO_2 with a 108 mAh g^{-1} capacity enhancement, which is close to the total enhanced capacity (126 mAh g^{-1}) compared with NBs−VO_2. NBs−VO_2 delivers an initial specific discharge capacity of 240 mAh g^{-1} at 100 mA g^{-1} but reduces in the subsequent two cycles (Figure 3d), showing a "dead Zn^{2+} sites" phenomenon which has been found in $Na_{0.33}V_2O_5$,[65] LiV_3O_8,[66] and V_2O_5[67] as cathodes for ZIBs.

https://dx.doi.org/10.1021/acsnano.9b09963
ACS Nano 2020, 14, 5581−5589

After that, the discharge capacity of NBs−VO_2 rises gradually, even recovering to 100 mA g^{-1} after rate cycling (Figure S9), giving rise to a maximum discharge capacity of 249 mAh g^{-1} in the first 10 cycles and 280 mAh g^{-1} after rate cycling. The gradually increasing discharge capacity and high Coulombic efficiency (>100%) demonstrate that the NBs−VO_2 has a gradual penetration of Zn^{2+} and activation process, like V_2O_5,[68,69] $H_2V_3O_8$,[70] suggesting the slow Zn^{2+} diffusion and intercalation kinetic and some irreversible processes in the NBs−VO_2. This phenomenon does not occur in $V_O^{\bullet\bullet}$−VO_2, which can quickly reach the maximum discharge capacity of 375 mAh g^{-1} and remain steady in the following cycles (Figure 3e). It is higher than that of the reported VO_2 nanofibers (357 mAh g^{-1}),[32] VO_2 nanorods (325 mAh g^{-1}),[33] RGO/VO_2 composite (276 mAh g^{-1}),[56] $Mg_xV_2O_5{\cdot}nH_2O$ (353 mAh g^{-1}),[63] and $Na_2V_6O_{16}{\cdot}3H_2O$ (361 mAh g^{-1}).[71] Compared with the NBs−VO_2, the enhanced galvanostatic charge−discharge performance of $V_O^{\bullet\bullet}$−VO_2 indicates that $V_O^{\bullet\bullet}$ facilitates zinc ion diffusion and intercalation, which might be ascribed to the expanded ion diffusion tunnels and increased active sites. EIS measurements show that $V_O^{\bullet\bullet}$−VO_2 has a lower charge transfer resistance than NBs−VO_2, demonstrating an improved charge transfer and ion diffusion in $V_O^{\bullet\bullet}$−VO_2 (Figure S10). The rate and cycling performance were also tested as shown in Figure S9a. The discharge capacity of 220 mAh g^{-1} is retained at 5 A g^{-1} for $V_O^{\bullet\bullet}$−VO_2, which is higher than that of NBs−VO_2 (186 mAh g^{-1}) (Figure S9b). Even at 8 A g^{-1}, the discharge capacity of $V_O^{\bullet\bullet}$−VO_2 is still maintained at 180 mAh g^{-1}. Figure 3f shows the long-term cyclic performance of NBs−VO_2 and $V_O^{\bullet\bullet}$−VO_2. After 2000 cycles, the $V_O^{\bullet\bullet}$−VO_2 exhibits a capacity of 175 mAh g^{-1} with a retention of 85% (with respect to the first cycle), higher than that of NBs−VO_2 (120 mAh g^{-1}, 65% retention), revealing that $V_O^{\bullet\bullet}$ is capable of improving the cycling stability of VO_2.

First-principles calculations were conducted. Apart from the VO_2 model, two modes with different contents of $V_O^{\bullet\bullet}$, $VO_{1.875}$, and $VO_{1.75}$ were built to discover a suitable model that agrees with the experimental XRD observations in Figures 2e,f. By analyzing the calculated XRD results and cell parameters (Figure S11, Table S1), $VO_{1.75}$ exhibited the same peak shift as observed in XRD characterization, (200) and (−601) peaks shift to lower angles (Figures 4a,b), while (110) peaks shift to larger angles (Figure S11) in contrast to VO_2. Therefore, VO_2 and $VO_{1.75}$ models were chosen to study the impacts of $V_O^{\bullet\bullet}$ on their electronic structures and zinc ion storage behavior. The similar trend of crystal structural changes of the $VO_{1.75}$ model with that of $V_O^{\bullet\bullet}$−VO_2 revealed that the as-obtained $V_O^{\bullet\bullet}$−VO_2 sample was in a high $V_O^{\bullet\bullet}$ concentration. The real oxygen vacancy content should be higher than that calculated by surface XPS ($VO_{1.86}$), as previously reported by Kim *et al.*[44] Combining calculated XRD patterns with the cell parameters (Figure S11, Table S1), it is confirmed that the $V_O^{\bullet\bullet}$ increase lattice parameters *a* and *c* from 11.947(9) and 6.435(8) Å in VO_2 to 12.344(4) and 6.503(6) Å in $VO_{1.75}$. It leads to expansion of the b tunnel in VO_2 and favors the ion diffusion.

Figures 4c,d and S12 show the density of state and band structure of the $VO_{1.75}$ and VO_2 models. Fermi levels residing in the conduction band reveal the metallic character of VO_2 and $VO_{1.75}$, which is in good agreement with the previous theoretical findings.[72,73] After introduction of $V_O^{\bullet\bullet}$, $VO_{1.75}$ exhibits a narrower bandgap than that of VO_2, which agrees well with the valence band XPS results in Figures 2c,d. Zn ion diffusion energy barriers in VO_2 and $VO_{1.75}$ were calculated by simulating the Zn ions diffusion along the b tunnel (Figure 4e). $VO_{1.75}$ presents a lower diffusion energy barrier (0.24−0.71 eV) than that of VO_2 (0.78 eV) when the zinc ions pass through the oxygen vacancy site (Figure 4f). Just like the trapping states, Zn ion passes through the $V_O^{\bullet\bullet}$, it will be trapped in this site and keep in a metastable state.[43] The lower migration energy barrier would enable the fast zinc ion diffusion along the b tunnel in the host lattice. The positive impact of $V_O^{\bullet\bullet}$ on the ion diffusion has also been verified by DFT method in $ZnMn_2O_4$,[43] $K_{0.8}Mn_8O_{16}$,[74] MoO_3,[44] and TiO_2.[60] Combining the theoretical calculation with the experimental observations, it is concluded that the creation of $V_O^{\bullet\bullet}$ could effectively boost the Zn storage performance of VO_2 (B).

CONCLUSIONS

Rich $V_O^{\bullet\bullet}$ resulted in an enlarged b tunnel and narrowed bandgap in VO_2 to enable fast charge transfer and ion diffusion, leading to improved electrochemical properties. The discharge capacity of 375 mAh g^{-1} at 100 mA g^{-1} was achieved in $V_O^{\bullet\bullet}$−VO_2, demonstrating a 34% capacity enhancement in comparison with NBs−VO_2 (280 mAh g^{-1} at 100 mA g^{-1}). DFT calculations confirms the expanded ion diffusion tunnel (along the *b* axis) and the reduced migration energy of zinc ions in $V_O^{\bullet\bullet}$-rich VO_2 compared with that of pristine VO_2. This work shows an efficient strategy to design $V_O^{\bullet\bullet}$-rich vanadium oxides as high-performance cathodes for aqueous zinc ion batteries.

EXPERIMENTAL SECTION

Material Preparation. VO_2 nanobelts (NBs−VO_2) were synthesized *via* solvothermal alcohol reduction reaction of V_2O_5. In a typical procedure, V_2O_5 (Sigma-Aldrich, 4 mmol) was dispersed in 50 mL of water/ethylene glycol (volume ratio: 3:2) mixture under vigorous stirring, transferred to a 100 mL autoclave, and kept in an oven at 200 °C for 6 h. After the reaction, the as-synthesized product was thoroughly washed with distilled water and ethanol several times and dried at 80 °C for 24 h.

As for the VO_2 nanosheets (NSs−VO_2) and $V_O^{\bullet\bullet}$−VO_2 samples, the commercial V_2O_5 would be substituted by V_2O_5 nanobelts (NBs−V_2O_5) (by annealing NBs−VO_2) and V_2O_5 nanosheets (NSs−V_2O_5) (by annealing NSs−VO_2), respectively.

NBs−V_2O_5 and NSs−V_2O_5 were obtained by annealing NBs−VO_2 and NSs−VO_2 in the air at 330 °C for 10 min with a heating rate of 2 °C min^{-1}, respectively.

Material Characterization. The powder XRD patterns were measured using a Rigaku SmartLab X-ray diffractometer 9 kW equipped with a D/teX Ultra 250 detector operating at 45 kV and 200 mA using Cu Kα radiation (λ = 1.540593) within a scanning angle, 2θ, range of 10−70° in steps of 0.01° using the Bragg−Brentano geometry. The morphologies of the samples were examined by a field-emission scanning electron microscope (FE-SEM, Helios Nanolab 600i, FEI). X-ray photoelectron spectroscopy (XPS) (ESCALAB 250, Thermo-VG Scientific) measurements were performed in macro mode (3 mm × 3 mm) to obtain information about the binding energy of the vanadium and valence band. The electron paramagnetic resonance (EPR) spectra were measured at 294 K with a Bruker EMX plus 10/12 (equipped with Oxford ESR910 Liquid Helium cryostat).

Electrochemical Measurements. Electrochemical experiments were performed using 2032-type coin cells within the voltage window of 0.3−1.5 V using a metallic Zn foil as the counter electrode. The working electrode was composed of 70 wt % active materials, 20 wt % Super P conductive additive, and 10 wt % polyvinylidene difluoride binder and was coated on a stainless-steel mesh and dried in air at 80 °C for 12 h. The mass loading of active materials is 2−3 mg/cm^2. The working and counter electrodes were separated by a piece of cellulose

https://dx.doi.org/10.1021/acsnano.9b09963
ACS Nano 2020, 14, 5581−5589

separator. The electrolyte used was 3 M $Zn(CF_3SO_3)_2$ aqueous solution because much better electrochemical performance has been certified using 3 M $Zn(CF_3SO_3)_2$ than other concentrations of $Zn(CF_3SO_3)_2$ and other Zn salts such as $ZnSO_4$, $Zn(NO_3)_2$. The cells were kept for 12 h before the electrochemical measurements. The discharge/charge measurements were performed using a Neware Battery Testing System (BTS 3000, Shenzhen Neware, China). Cyclic voltammograms (CV) were tested on an electrochemical workstation (CHI600E). The electrochemical impedance spectra (EIS) were measured at frequencies from 100 kHz to 100 mHz, amplitude voltage of 10 mV with a Solartron 1260 Multistat impedance analyzer. Obtained spectra were analyzed by equivalent circuits using ZView2 electrochemical impedance software (Scribner Associates Inc.). All of the tests were measured at room temperature.

First-Principles Calculations. The primitive VO_2 is a monoclinic structure with space group $C12/m1$, which possesses 8 V atoms and 16 O atoms with lattice parameters a = 11.9479 Å, b = 3.7189 Å, c = 6.4358 Å. The configurations with $V_O^{\bullet\bullet}$ were obtained by deleting the appropriate amount of oxygen atoms. XRD and projected density of states calculations were performed using the Cambridge Serial Total Energy Package (CASTEP) program.[75,76] The generalized gradient approximation (GGA) in the scheme of Perdew−Burke−Ernzerhof (PBE) function was applied to calculate the electron exchange-correlation interactions.[77] Ultrasoft pseudopotentials for V and O were used. Cutoff energy of 340 eV according to the fine quality set by software self-recommendation. A Monkhorst−Pack k-point scheme was set as 1 × 4 × 2 to geometry optimization. The convergence tolerances for geometry optimization calculations with spin fully able to relax for all steps were set to a maximum displacement of 1.0×10^{-3} Å, a maximum force of 0.03 eV/Å, a maximum energy change of 1.0×10^{-6} eV/atom, and maximum stress of 0.05 GPa. In addition, Koelling−Harmon relativistic effect was considered in the calculation process.

Then Nudged elastic band (NEB) calculations were performed by the Vienna *Ab initio* Simulation Package (VASP) to determine the activation barrier of Zn^{2+} ion diffusion in the optimized structure.[78−80] The VO_2 and $VO_{1.75}$ configurations were chosen as the research targets, a supercell consists of 32 formula units of VO_2, and one Zn ion was added along the b tunnel to simulate the diffusion. Five intermediate states between its initial and final positions were carried out. All the structures were allowed to relax within the fixed lattice parameters, which is similar to the method reported by Park *et al.*[64]

ASSOCIATED CONTENT

Supporting Information

The Supporting Information is available free of charge at https://pubs.acs.org/doi/10.1021/acsnano.9b09963.

Additional synthesis details, materials characterization, electrochemical data, and DFT calculation results (PDF)

AUTHOR INFORMATION

Corresponding Authors

Linhua Hu − *Key Laboratory of Photovoltaic and Energy Conservation Materials, CAS, Institute of Applied Technology, Hefei Institutes of Physical Science, Chinese Academy of Sciences, Hefei, Anhui 230031, P.R. China;* orcid.org/0000-0002-0513-2999; Email: lhhu@rntek.cas.cn

Denghui Ji − *College of Physics, Mechanical and Electronical College, Shijiazhuang University, Shijiazhuang City 050035, P.R. China*; Email: jidenghui2007@163.com

Guozhong Cao − *Department of Materials Science and Engineering, University of Washington, Seattle, Washington 98195, United States;* orcid.org/0000-0001-6539-0490; Email: gzcao@u.washington.edu

Authors

Zhaoqian Li − *Key Laboratory of Photovoltaic and Energy Conservation Materials, CAS, Institute of Applied Technology, Hefei Institutes of Physical Science, Chinese Academy of Sciences, Hefei, Anhui 230031, P.R. China; Department of Materials Science and Engineering, University of Washington, Seattle, Washington 98195, United States;* orcid.org/0000-0002-9809-4097

Yingke Ren − *College of Science, Hebei University of Science and Technology, Shijiazhuang 050018, P.R. China*

Lie Mo − *Key Laboratory of Photovoltaic and Energy Conservation Materials, CAS, Institute of Applied Technology, Hefei Institutes of Physical Science, Chinese Academy of Sciences, Hefei, Anhui 230031, P.R. China*

Chaofeng Liu − *Department of Materials Science and Engineering, University of Washington, Seattle, Washington 98195, United States*

Kevin Hsu − *Department of Materials Science and Engineering, University of Washington, Seattle, Washington 98195, United States*

Youcai Ding − *Key Laboratory of Photovoltaic and Energy Conservation Materials, CAS, Institute of Applied Technology, Hefei Institutes of Physical Science, Chinese Academy of Sciences, Hefei, Anhui 230031, P.R. China*

Xianxi Zhang − *Shandong Provincial Key Laboratory/Collaborative Innovation Center of Chemical Energy Storage & Novel Cell Technology, School of Chemistry and Chemical Engineering, Liaocheng University, Liaocheng 252000, P.R. China;* orcid.org/0000-0002-2900-9469

Xiuling Li − *College of Physics and Information Engineering, Hebei Advanced Thin Films Laboratory, Hebei Normal University, Shijiazhuang City 050024, P.R. China*

Complete contact information is available at: https://pubs.acs.org/10.1021/acsnano.9b09963

Author Contributions

Z.L., L.H., and G.C. conceived the idea. Z.L., L.M., C.L., K.H., and Y.D. synthesized the materials and performed materials characterization and electrochemistry measurements. Y.R., D.J., X.Z., and X.L. performed the density functional theory analysis. Z.L., L.H., and G.C. wrote the paper with critical input from all other authors. All authors edited and approved the manuscript.

Notes

The authors declare no competing financial interest.

ACKNOWLEDGMENTS

This work was supported by the National Key R&D Program of China (No. 2019YFB1503200), the National Key R&D Program of China (No. 2017YFE0133800), the National Science Foundation (No. CBET-1803256), the Anhui Provincial Natural Science Foundation (No. 1908085QB52), the CASHIPS Director's Fund (No. YZJJ201902 and YZJJ2018QN21), the Key Technology R&D Program of Jiangxi Province (No. 20181ACH80010), Colleges and Universities in Shandong Province science and technology projects (No. J17KA097), China Scholarship Council International Clean Energy Talent program, and CAS Key Laboratory of Photovoltaic and Energy Conservation, Chinese Academy of Sciences (No. PECL2018QN006). A portion of this work was performed at the Steady High Magnetic Field Facilities, High Magnetic Field Laboratory, Chinese Academy of Sciences.

REFERENCES

(1) Pan, H. L.; Shao, Y. Y.; Yan, P. F.; Cheng, Y. W.; Han, K. S.; Nie, Z. M.; Wang, C. M.; Yang, J. H.; Li, X. L.; Bhattacharya, P.; Mueller, K. T.; Liu, J. Reversible Aqueous Zinc/Manganese Oxide Energy Storage from Conversion Reactions. *Nat. Energy* **2016**, *1*, 1−7.

(2) Tang, B. Y.; Shan, L. T.; Liang, S. Q.; Zhou, J. Issues and Opportunities Facing Aqueous Zinc-Ion Batteries. *Energy Environ. Sci.* **2019**, *12*, 3288−3304.

(3) Wu, Y. P.; Gong, M.; Lin, M. C.; Yuan, C. Z.; Angell, M.; Huang, L.; Wang, D. Y.; Zhang, X. D.; Yang, J.; Hwang, B. J.; Dai, H. J. 3D Graphitic Foams Derived from Chloroaluminate Anion Intercalation for Ultrafast Aluminum-Ion Battery. *Adv. Mater.* **2016**, *28*, 9218−9222.

(4) Tepavcevic, S.; Liu, Y. Z.; Zhou, D. H.; Lai, B.; Maser, J.; Zuo, X. B.; Chan, H.; Kral, P.; Johnson, C. S.; Stamenkovic, V.; Markovic, N. M.; Rajh, T. Nanostructured Layered Cathode for Rechargeable Mg-Ion Batteries. *ACS Nano* **2015**, *9*, 8194−8205.

(5) Sun, W.; Wang, F.; Hou, S. Y.; Yang, C. Y.; Fan, X. L.; Ma, Z. H.; Gao, T.; Han, F. D.; Hu, R. Z.; Zhu, M.; Wang, C. S. Zn/MnO_2 Battery Chemistry with H^+ and Zn^{2+} Coinsertion. *J. Am. Chem. Soc.* **2017**, *139*, 9775−9778.

(6) Zhang, N.; Cheng, F. Y.; Liu, J. X.; Wang, L. B.; Long, X. H.; Liu, X. S.; Li, F. J.; Chen, J. Rechargeable Aqueous Zinc-Manganese Dioxide Batteries with High Energy and Power Densities. *Nat. Commun.* **2017**, *8*, 1−9.

(7) Liu, C.; Neale, Z.; Zheng, J.; Jia, X.; Huang, J.; Yan, M.; Tian, M.; Wang, M.; Yang, J.; Cao, G. Expanded Hydrated Vanadate for High-Performance Aqueous Zinc-Ion Batteries. *Energy Environ. Sci.* **2019**, *12*, 2273−2285.

(8) Wu, Y. Z.; Wang, M. C.; Tao, Y.; Zhang, K.; Cai, M. L.; Ding, Y.; Liu, X. P.; Hayat, T.; Alsaedi, A.; Dai, S. Y. Electrochemically Derived Graphene-Like Carbon Film as a Superb Substrate for High-Performance Aqueous Zn-Ion Batteries. *Adv. Funct. Mater.* **2020**, *30*, 1907120.

(9) Xia, C.; Guo, J.; Li, P.; Zhang, X. X.; Alshareef, H. N. Highly Stable Aqueous Zinc-Ion Storage Using a Layered Calcium Vanadium Oxide Bronze Cathode. *Angew. Chem., Int. Ed.* **2018**, *57*, 3943−3948.

(10) Kundu, D.; Adams, B. D.; Duffort, V.; Vajargah, S. H.; Nazar, L. F. A High-Capacity and Long-Life Aqueous Rechargeable Zinc Battery Using a Metal Oxide Intercalation Cathode. *Nat. Energy* **2016**, *1*, 16119.

(11) Guo, S.; Liang, S.; Zhang, B.; Fang, G.; Ma, D.; Zhou, J. Cathode Interfacial Layer Formation *via In Situ* Electrochemically Charging in Aqueous Zinc-Ion Battery. *ACS Nano* **2019**, *13*, 13456−13464.

(12) Song, M.; Tan, H.; Chao, D. L.; Fan, H. J. Recent Advances in Zn-Ion Batteries. *Adv. Funct. Mater.* **2018**, *28*, 1802564.

(13) Mo, F. N.; Liang, G. J.; Meng, Q. Q.; Liu, Z. X.; Li, H. F.; Fan, J.; Zhi, C. Y. A Flexible Rechargeable Aqueous Zinc Manganese-Dioxide Battery Working at −20 °C. *Energy Environ. Sci.* **2019**, *12*, 706−715.

(14) Wang, D. H.; Wang, L. F.; Liang, G. J.; Li, H. F.; Liu, Z. X.; Tang, Z. J.; Liang, J. B.; Zhi, C. Y. A Superior δ-MnO_2 Cathode and a Self-Healing Zn-δ-MnO_2 Battery. *ACS Nano* **2019**, *13*, 10643−10652.

(15) Li, Y.; Huang, Z.; Kalambate, P. K.; Zhong, Y.; Huang, Z.; Xie, M.; Shen, Y.; Huang, Y. V_2O_5 Nanopaper as a Cathode Material with High Capacity and Long Cycle Life for Rechargeable Aqueous Zinc-Ion Battery. *Nano Energy* **2019**, *60*, 752−759.

(16) Ding, Y.; Peng, Y.; Chen, S.; Zhang, X.; Li, Z.; Zhu, L.; Mo, L.-E.; Hu, L. Hierarchical Porous Metallic V_2O_3@C for Advanced Aqueous Zinc-Ion Batteries. *ACS Appl. Mater. Interfaces* **2019**, *11*, 44109−44117.

(17) Ding, Y. C.; Peng, Y. Q.; Chen, W. Y.; Niu, Y. J.; Wu, S. G.; Zhang, X. X.; Hu, L. H. V-MOF Derived Porous V_2O_5 Nanoplates for High Performance Aqueous Zinc Ion Battery. *Appl. Surf. Sci.* **2019**, *493*, 368−374.

(18) Liu, Y. Y.; Li, Q.; Ma, K. X.; Yang, G. Z.; Wang, C. X. Graphene Oxide Wrapped CuV_2O_6 Nanobelts as High-Capacity and Long-Life Cathode Materials of Aqueous Zinc-Ion Batteries. *ACS Nano* **2019**, *13*, 12081−12089.

(19) Pan, Z. H.; Yang, J.; Yang, J.; Zhang, Q. C.; Zhang, H.; Li, X.; Kou, Z. K.; Zhang, Y. F.; Chen, H.; Yan, C. L.; Wang, J. Stitching of $Zn_3(OH)_2V_2O_7{\cdot}2H_2O$ 2D Nanosheets by 1D Carbon Nanotubes Boosts Ultrahigh Rate for Wearable Quasi-Solid-State Zinc-Ion Batteries. *ACS Nano* **2020**, *14*, 842−853.

(20) Kasiri, G.; Glenneberg, J.; Hashemi, A. B.; Kun, R.; La Mantia, F. Mixed Copper-Zinc Hexacyanoferrates as Cathode Materials for Aqueous Zinc-Ion Batteries. *Energy Storage Mater.* **2019**, *19*, 360−369.

(21) Liu, Z.; Pulletikurthi, G.; Endres, F. A Prussian Blue/Zinc Secondary Battery with a Bio-Ionic Liquid−Water Mixture as Electrolyte. *ACS Appl. Mater. Interfaces* **2016**, *8*, 12158−12164.

(22) Kasiri, G.; Trócoli, R.; Bani Hashemi, A.; La Mantia, F. An Electrochemical Investigation of the Aging of Copper Hexacyanoferrate during the Operation in Zinc-Ion Batteries. *Electrochim. Acta* **2016**, *222*, 74−83.

(23) Trocoli, R.; La Mantia, F. An Aqueous Zinc-Ion Battery Based on Copper Hexacyanoferrate. *ChemSusChem* **2015**, *8*, 481−485.

(24) Cheng, Y.; Luo, L.; Zhong, L.; Chen, J.; Li, B.; Wang, W.; Mao, S. X.; Wang, C.; Sprenkle, V. L.; Li, G.; Liu, J. Highly Reversible Zinc-Ion Intercalation into Chevrel Phase Mo_6S_8 Nanocubes and Applications for Advanced Zinc-Ion Batteries. *ACS Appl. Mater. Interfaces* **2016**, *8*, 13673−13677.

(25) Chae, M. S.; Heo, J. W.; Lim, S.-C.; Hong, S.-T. Electrochemical Zinc-Ion Intercalation Properties and Crystal Structures of $ZnMo_6S_8$ and $Zn_2Mo_6S_8$ Chevrel Phases in Aqueous Electrolytes. *Inorg. Chem.* **2016**, *55*, 3294−3301.

(26) Zhao, Q.; Huang, W. W.; Luo, Z. Q.; Liu, L. J.; Lu, Y.; Li, Y. X.; Li, L.; Hu, J. Y.; Ma, H.; Chen, J. High-Capacity Aqueous Zinc Batteries Using Sustainable Quinone Electrodes. *Sci. Adv.* **2018**, *4*, eaao1761.

(27) Kundu, D.; Oberholzer, P.; Glaros, C.; Bouzid, A.; Tervoort, E.; Pasquarello, A.; Niederberger, M. Organic Cathode for Aqueous Zn-Ion Batteries: Taming a Unique Phase Evolution toward Stable Electrochemical Cycling. *Chem. Mater.* **2018**, *30*, 3874−3881.

(28) Yang, S. B.; Gong, Y. J.; Liu, Z.; Zhan, L.; Hashim, D. P.; Ma, L. L.; Vajtai, R.; Ajayan, P. M. Bottom-Up Approach toward Single-Crystalline VO_2-Graphene Ribbons as Cathodes for Ultrafast Lithium Storage. *Nano Lett.* **2013**, *13*, 1596−1601.

(29) Chao, D. L.; Zhu, C. R.; Xia, X. H.; Liu, J. L.; Zhang, X.; Wang, J.; Liang, P.; Lin, J. Y.; Zhang, H.; Shen, Z. X.; Fan, H. J. Graphene Quantum Dots Coated VO_2 Arrays for Highly Durable Electrodes for Li and Na Ion Batteries. *Nano Lett.* **2015**, *15*, 565−573.

(30) Li, Z. L.; Ganapathy, S.; Xu, Y. L.; Zhou, Z.; Sarilar, M.; Wagemaker, M. Mechanistic Insight into the Electrochemical Performance of Zn/VO_2 Batteries with an Aqueous $ZnSO_4$ Electrolyte. *Adv. Energy Mater.* **2019**, *9*, 1900237.

(31) Wei, T. Y.; Li, Q.; Yang, G. Z.; Wang, C. X. An Electrochemically Induced Bilayered Structure Facilitates Long-Life Zinc Storage of Vanadium Dioxide. *J. Mater. Chem. A* **2018**, *6*, 8006−8012.

(32) Ding, J. W.; Du, Z. G.; Gu, L. Q.; Li, B.; Wang, L. Z.; Wang, S. W.; Gong, Y. J.; Yang, S. B. Ultrafast Zn^{2+} Intercalation and Deintercalation in Vanadium Dioxide. *Adv. Mater.* **2018**, *30*, 1800762.

(33) Chen, L. N.; Ruan, Y. S.; Zhang, G. B.; Wei, Q. L.; Jiang, Y. L.; Xiong, T. F.; He, P.; Yang, W.; Yan, M. Y.; An, Q. Y.; Mai, L. Q. Ultrastable and High-Performance Zn/VO_2 Battery Based on a Reversible Single-Phase Reaction. *Chem. Mater.* **2019**, *31*, 699−706.

(34) Wan, F.; Niu, Z. Q. Design Strategies for Vanadium-Based Aqueous Zinc-Ion Batteries. *Angew. Chem., Int. Ed.* **2019**, *58*, 16358−16367.

(35) Hu, P.; Zhu, T.; Wang, X.; Wei, X.; Yan, M.; Li, J.; Luo, W.; Yang, W.; Zhang, W.; Zhou, L.; Zhou, Z.; Mai, L. Highly Durable $Na_2V_6O_{16}{\cdot}1.63H_2O$ Nanowire Cathode for Aqueous Zinc-Ion Battery. *Nano Lett.* **2018**, *18*, 1758−1763.

(36) Sambandam, B.; Soundharrajan, V.; Kim, S.; Alfaruqi, M. H.; Jo, J.; Kim, S.; Mathew, V.; Sun, Y.-k.; Kim, J. $K_2V_6O_{16}{\cdot}2.7H_2O$

https://dx.doi.org/10.1021/acsnano.9b09963
ACS Nano 2020, 14, 5581−5589

Nanorod Cathode: An Advanced Intercalation System for High Energy Aqueous Rechargeable Zn-Ion Batteries. *J. Mater. Chem. A* **2018**, *6*, 15530−15539.
(37) Wang, F.; Sun, W.; Shadike, Z.; Hu, E. Y.; Ji, X.; Gao, T.; Yang, X. Q.; Xu, K.; Wang, C. S. How Water Accelerates Bivalent Ion Diffusion at the Electrolyte/Electrode Interface. *Angew. Chem., Int. Ed.* **2018**, *57*, 11978−11981.
(38) Yan, M.; He, P.; Chen, Y.; Wang, S.; Wei, Q.; Zhao, K.; Xu, X.; An, Q.; Shuang, Y.; Shao, Y.; Mueller, K. T.; Mai, L.; Liu, J.; Yang, J. Water-Lubricated Intercalation in $V_2O_5{\cdot}nH_2O$ for High-Capacity and High-Rate Aqueous Rechargeable Zinc Batteries. *Adv. Mater.* **2018**, *30*, 1703725.
(39) Xiong, T.; Yu, Z. G.; Wu, H. J.; Du, Y. H.; Xie, Q. D.; Chen, J. S.; Zhang, Y. W.; Pennycook, S. J.; Lee, W. S. V.; Xue, J. M. Defect Engineering of Oxygen-Deficient Manganese Oxide to Achieve High-Performing Aqueous Zinc Ion Battery. *Adv. Energy Mater.* **2019**, *9*, 1803815.
(40) Liao, M.; Wang, J.; Ye, L.; Sun, H.; Wen, Y.; Wang, C.; Sun, X.; Wang, B.; Peng, H. A Deep-Cycle Aqueous Zinc-Ion Battery Containing an Oxygen-Deficient Vanadium Oxide Cathode. *Angew. Chem., Int. Ed.* **2020**, *59*, 2273−2278.
(41) Han, M.; Huang, J.; Liang, S.; Shan, L.; Xie, X.; Yi, Z.; Wang, Y.; Guo, S.; Zhou, J. Oxygen Defects in β-MnO_2 Enabling High-Performance Rechargeable Aqueous Zinc/Manganese Dioxide Battery. *iScience* **2020**, *23*, 100797.
(42) Zeng, Y. X.; Lai, Z. Z.; Han, Y.; Zhang, H. Z.; Xie, S. L.; Lu, X. H. Oxygen-Vacancy and Surface Modulation of Ultrathin Nickel Cobaltite Nanosheets as a High-Energy Cathode for Advanced Zn-Ion Batteries. *Adv. Mater.* **2018**, *30*, 1802396.
(43) Zhang, H.; Wang, J.; Liu, Q.; He, W.; Lai, Z.; Zhang, X.; Yu, M.; Tong, Y.; Lu, X. Extracting Oxygen Anions from $ZnMn_2O_4$: Robust Cathode for Flexible All-Solid-State Zn-Ion Batteries. *Energy Storage Mater.* **2019**, *21*, 154−161.
(44) Kim, H. S.; Cook, J. B.; Lin, H.; Ko, J. S.; Tolbert, S. H.; Ozolins, V.; Dunn, B. Oxygen Vacancies Enhance Pseudocapacitive Charge Storage Properties of MoO_{3-x}. *Nat. Mater.* **2017**, *16*, 454−460.
(45) Ni, Q.; Dong, R.; Bai, Y.; Wang, Z.; Ren, H.; Sean, S.; Wu, F.; Xu, H.; Wu, C. Superior Sodium-Storage Behavior of Flexible Anatase TiO_2 Promoted by Oxygen Vacancies. *Energy Storage Mater.* **2020**, *25*, 903−911.
(46) Pan, A. Q.; Wu, H. B.; Yu, L.; Lou, X. W. Template-Free Synthesis of VO_2 Hollow Microspheres with Various Interiors and Their Conversion into V_2O_5 for Lithium-Ion Batteries. *Angew. Chem., Int. Ed.* **2013**, *52*, 2226−2230.
(47) Liu, Y. Y.; Uchaker, E.; Zhou, N.; Li, J. G.; Zhang, Q. F.; Cao, G. Z. Facile Synthesis of Nanostructured Vanadium Oxide as Cathode Materials for Efficient Li-Ion Batteries. *J. Mater. Chem.* **2012**, *22*, 24439−24445.
(48) Occhiuzzi, M.; Cordischi, D.; Dragone, R. Reactivity of Some Vanadium Oxides: An EPR and XRD Study. *J. Solid State Chem.* **2005**, *178*, 1551−1558.
(49) Krzystek, J.; Ozarowski, A.; Telser, J.; Crans, D. C. High-Frequency and -Field Electron Paramagnetic Resonance of Vanadium (IV, III, and II) Complexes. *Coord. Chem. Rev.* **2015**, *301*, 123−133.
(50) Wang, Q. S.; Zhang, Y. F.; Zheng, J. Q.; Hu, T.; Meng, C. G. Synthesis, Structure, Optical and Magnetic Properties of Interlamellar Decoration of Magadiite Using Vanadium Oxide Species. *Microporous Mesoporous Mater.* **2017**, *244*, 264−277.
(51) Adamski, A.; Spalek, T.; Sojka, Z. Application of EPR Spectroscopy for Elucidation of Vanadium Speciation in VO_x/ZrO_2 Catalysts Subject to Redox Treatment. *Res. Chem. Intermed.* **2003**, *29*, 793−804.
(52) Liu, B.-T.; Shi, X.-M.; Lang, X.-Y.; Gu, L.; Wen, Z.; Zhao, M.; Jiang, Q. Extraordinary Pseudocapacitive Energy Storage Triggered by Phase Transformation in Hierarchical Vanadium Oxides. *Nat. Commun.* **2018**, *9*, 1375.
(53) Xu, H. Y.; Huang, Y. H.; Liu, S.; Xu, K. W.; Ma, F.; Chu, P. K. Effects of Annealing Ambient on Oxygen Vacancies and Phase Transition Temperature of VO_2 Thin Films. *RSC Adv.* **2016**, *6*, 79383−79388.
(54) Moatti, A.; Sachan, R.; Gupta, S.; Narayan, J. Vacancy-Driven Robust Metallicity of Structurally Pinned Monoclinic Epitaxial VO_2 Thin Films. *ACS Appl. Mater. Interfaces* **2019**, *11*, 3547−3554.
(55) Zhao, J.; Ren, H.; Liang, Q.; Yuan, D.; Xi, S.; Wu, C.; Manalastas, W.; Ma, J.; Fang, W.; Zheng, Y.; Du, C.-F.; Srinivasan, M.; Yan, Q. High-Performance Flexible Quasi-Solid-State Zinc-Ion Batteries with Layer-Expanded Vanadium Oxide Cathode and Zinc/Stainless Steel Mesh Composite Anode. *Nano Energy* **2019**, *62*, 94−102.
(56) Dai, X.; Wan, F.; Zhang, L. L.; Cao, H. M.; Niu, Z. Q. Freestanding Graphene/VO_2 Composite Films for Highly Stable Aqueous Zn-Ion Batteries with Superior Rate Performance. *Energy Storage Mater.* **2019**, *17*, 143−150.
(57) Chen, X. B.; Liu, L.; Yu, P. Y.; Mao, S. S. Increasing Solar Absorption for Photocatalysis with Black Hydrogenated Titanium Dioxide Nanocrystals. *Science* **2011**, *331*, 746−750.
(58) Naldoni, A.; Allieta, M.; Santangelo, S.; Marelli, M.; Fabbri, F.; Cappelli, S.; Bianchi, C. L.; Psaro, R.; Dal Santo, V. Effect of Nature and Location of Defects on Bandgap Narrowing in Black TiO_2 Nanoparticles. *J. Am. Chem. Soc.* **2012**, *134*, 7600−7603.
(59) Chen, J.; Ding, Z.; Wang, C.; Hou, H.; Zhang, Y.; Wang, C.; Zou, G.; Ji, X. Black Anatase Titania with Ultrafast Sodium-Storage Performances Stimulated by Oxygen Vacancies. *ACS Appl. Mater. Interfaces* **2016**, *8*, 9142−9151.
(60) Zhang, Y.; Ding, Z.; Foster, C. W.; Banks, C. E.; Qiu, X.; Ji, X. Oxygen Vacancies Evoked Blue TiO_2(B) Nanobelts with Efficiency Enhancement in Sodium Storage Behaviors. *Adv. Funct. Mater.* **2017**, *27*, 1700856.
(61) Qiu, J.; Li, S.; Gray, E.; Liu, H.; Gu, Q.-F.; Sun, C.; Lai, C.; Zhao, H.; Zhang, S. Hydrogenation Synthesis of Blue TiO_2 for High-Performance Lithium-Ion Batteries. *J. Phys. Chem. C* **2014**, *118*, 8824−8830.
(62) Liao, H. X.; Xie, L. L.; Zhang, Y.; Qiu, X. Q.; Li, S. M.; Huang, Z. D.; Hou, H. S.; Ji, X. B. Mo-Doped Gray Anatase TiO_2: Lattice Expansion for Enhanced Sodium Storage. *Electrochim. Acta* **2016**, *219*, 227−234.
(63) Ming, F. W.; Liang, H. F.; Lei, Y. J.; Kandambeth, S.; Eddaoudi, M.; Alshareef, H. N. Layered $Mg_xV_2O_5{\cdot}nH_2O$ as Cathode Material for High-Performance Aqueous Zinc Ion Batteries. *ACS Energy Lett.* **2018**, *3*, 2602−2609.
(64) Park, J. S.; Jo, J. H.; Aniskevich, Y.; Bakavets, A.; Ragoisha, G.; Streltsov, E.; Kim, J.; Myung, S. T. Open-Structured Vanadium Dioxide as an Intercalation Host for Zn Ions: Investigation by First-Principles Calculation and Experiments. *Chem. Mater.* **2018**, *30*, 6777−6787.
(65) He, P.; Zhang, G. B.; Liao, X. B.; Yan, M. Y.; Xu, X.; An, Q. Y.; Liu, J.; Mai, L. Q. Sodium Ion Stabilized Vanadium Oxide Nanowire Cathode for High-Performance Zinc-Ion Batteries. *Adv. Energy Mater.* **2018**, *8*, 1702463.
(66) Alfaruqi, M. H.; Mathew, V.; Song, J.; Kim, S.; Islam, S.; Pham, D. T.; Jo, J.; Kim, S.; Baboo, J. P.; Xiu, Z.; Lee, K.-S.; Sun, Y.-K.; Kim, J. Electrochemical Zinc Intercalation in Lithium Vanadium Oxide: A High-Capacity Zinc-Ion Battery Cathode. *Chem. Mater.* **2017**, *29*, 1684−1694.
(67) Senguttuvan, P.; Han, S.-D.; Kim, S.; Lipson, A. L.; Tepavcevic, S.; Fister, T. T.; Bloom, I. D.; Burrell, A. K.; Johnson, C. S. A High Power Rechargeable Nonaqueous Multivalent Zn/V_2O_5 Battery. *Adv. Energy Mater.* **2016**, *6*, 1600826.
(68) Zhang, N.; Dong, Y.; Jia, M.; Bian, X.; Wang, Y.; Qiu, M.; Xu, J.; Liu, Y.; Jiao, L.; Cheng, F. Rechargeable Aqueous Zn−V_2O_5 Battery with High Energy Density and Long Cycle Life. *ACS Energy Lett.* **2018**, *3*, 1366−1372.
(69) Hu, P.; Yan, M.; Zhu, T.; Wang, X.; Wei, X.; Li, J.; Zhou, L.; Li, Z.; Chen, L.; Mai, L. Zn/V_2O_5 Aqueous Hybrid-Ion Battery with High Voltage Platform and Long Cycle Life. *ACS Appl. Mater. Interfaces* **2017**, *9*, 42717−42722.

https://dx.doi.org/10.1021/acsnano.9b09963
ACS Nano 2020, 14, 5581−5589

(70) Pang, Q.; Sun, C.; Yu, Y.; Zhao, K.; Zhang, Z.; Voyles, P. M.; Chen, G.; Wei, Y.; Wang, X. $H_2V_3O_8$ Nanowire/Graphene Electrodes for Aqueous Rechargeable Zinc Ion Batteries with High Rate Capability and Large Capacity. *Adv. Energy Mater.* **2018**, *8*, 1800144.
(71) Soundharrajan, V.; Sambandam, B.; Kim, S.; Alfaruqi, M. H.; Putro, D. Y.; Jo, J.; Kim, S.; Mathew, V.; Sun, Y.-K.; Kim, J. $Na_2V_6O_{16}\cdot 3H_2O$ Barnesite Nanorod: An Open Door to Display a Stable and High Energy for Aqueous Rechargeable Zn-Ion Batteries as Cathodes. *Nano Lett.* **2018**, *18*, 2402−2410.
(72) Brito, W. H.; Aguiar, M. C. O.; Haule, K.; Kotliar, G. Metal-Insulator Transition in VO_2: A DFT + DMFT Perspective. *Phys. Rev. Lett.* **2016**, *117*, No. 056402.
(73) Abdellaoui, I.; Merad, G.; Maaza, M.; Abdelkader, H. S. Electronic and Optical Properties of Mg-, F-Doped and Mg\F-Codoped M-1−VO_2 *via* Hybrid Density Functional Calculations. *J. Alloys Compd.* **2016**, *658*, 569−575.
(74) Fang, G.; Zhu, C.; Chen, M.; Zhou, J.; Tang, B.; Cao, X.; Zheng, X.; Pan, A.; Liang, S. Suppressing Manganese Dissolution in Potassium Manganate with Rich Oxygen Defects Engaged High-Energy-Density and Durable Aqueous Zinc-Ion Battery. *Adv. Funct. Mater.* **2019**, *29*, 1808375.
(75) Milman, V.; Winkler, B.; White, J. A.; Pickard, C. J.; Payne, M. C.; Akhmatskaya, E. V.; Nobes, R. H. Electronic Structure, Properties, and Phase Stability of Inorganic Crystals: A Pseudopotential Plane-Wave Study. *Int. J. Quantum Chem.* **2000**, *77*, 895−910.
(76) Clark, S. J.; Segall, M. D.; Pickard, C. J.; Hasnip, P. J.; Probert, M. J.; Refson, K.; Payne, M. C. First Principles Methods Using CASTEP. *Z. Kristallogr. - Cryst. Mater.* **2005**, *220*, 567−570.
(77) Perdew, J. P.; Burke, K.; Ernzerhof, M. Generalized Gradient Approximation Made Simple. *Phys. Rev. Lett.* **1996**, *77*, 3865−3868.
(78) Henkelman, G.; Uberuaga, B. P.; Jonsson, H. A Climbing Image Nudged Elastic Band Method for Finding Saddle Points and Minimum Energy Paths. *J. Chem. Phys.* **2000**, *113*, 9901−9904.
(79) Kresse, G.; Furthmuller, J. Efficient Iterative Schemes for *Ab Initio* Total-Energy Calculations Using a Plane-Wave Basis Set. *Phys. Rev. B: Condens. Matter Mater. Phys.* **1996**, *54*, 11169−11186.
(80) Kresse, G.; Furthmuller, J. Efficiency of *Ab-Initio* Total Energy Calculations for Metals and Semiconductors Using a Plane-Wave Basis Set. *Comput. Mater. Sci.* **1996**, *6*, 15−50.

https://dx.doi.org/10.1021/acsnano.9b09963
ACS Nano 2020, 14, 5581−5589